



Structure and mechanical properties of low-density AlCrFeTiX (X = Co, Ni, Cu) high-entropy alloys produced by spark plasma sintering

N. Yurchenko^{a,b,*}, D. Shaysultanov^b, E. Povolyaeva^{a,b}, D. Moskovskikh^c, S. Zhrebtsov^{a,b}, N. Stepanov^{a,b}

^a World-Class Research Center “Advanced Digital Technologies”, State Marine Technical University, Saint Petersburg 198095, Russia

^b Belgorod National Research University, Belgorod 308015, Russia

^c National University of Science and Technology MISiS, Moscow 119049, Russia

ARTICLE INFO

Keywords:

High-entropy alloys
Low-density
Spark plasma sintering
Structure
Mechanical properties

ABSTRACT

In this study, low-density ($< 6 \text{ g/cm}^3$) AlCrFeTiX (x = Co, Ni, Cu) high-entropy alloys were produced by mechanical alloying and spark plasma sintering (SPS), and their structures and mechanical properties after SPS and annealing at 1000 °C for 24 h were reported. Both after SPS and annealing, the AlCrFeTiX (x = Co, Ni, Cu) alloys consisted of an L2₁ matrix phase with embedded bcc and C14 Laves phase particles. All the alloys had a nano-sized structure after SPS that retained in the AlCrFeTiCo and AlCrFeTiNi alloys after annealing. In the AlCrFeTiCu alloy, the annealing led to a coarsening, with an increase in the size of structural constituents above 1 μm. Compression tests showed that the AlCrFeTiX (x = Co, Ni, Cu) alloys after SPS were brittle at 25 °C, but the AlCrFeTiCo alloy exhibited the highest peak strength of 3792 MPa. At 600 °C, the AlCrFeTiCo alloy after SPS also demonstrated the best performance, with the yield strength, peak strength, and plastic strain of 1960 MPa, 2121 MPa, and 1.8 %, respectively. The annealing did not eliminate the room-temperature brittleness, but improved the mechanical properties at 600 °C. The AlCrFeTiCo alloy showed a 15 % increase in yield strength (2264 MPa) and more than 2.5 times higher compressive plasticity (4.7 %). The AlCrFeTiNi alloy became more ductile (1 %) and stronger (2200 MPa). For the AlCrFeTiCu alloy, the annealing had a negative effect that resulted in a halved plasticity at 600 °C. The AlCrFeTiCo and AlCrFeTiNi alloys after annealing showed record-high specific yield strength values at 600 °C, which were 383 and 371 MPa·cm³/g, respectively. With these values, the AlCrFeTiCo and AlCrFeTiNi alloys outperformed all the low-density medium-/high-entropy alloys available in literature to date obtained both by SPS or conventional casting. The structure formation and mechanical properties, as well as the response of these features to annealing, were extensively discussed.

1. Introduction

Materials that can combine low density and high strength are always demanding in the industry, especially in the aerospace sector, where the strength-to-weight ratio plays a decisive role [1]. To date, the most widespread low-density alloys are Al and Ti alloys [2–4]. However, despite these alloys being workhorses for many applications, the further improvement of their properties, like increasing the operating temperature, required for next-generation aircraft, remains elusive because of the traditional one-base-element approach. A brand new concept of high/medium-entropy alloys (HEAs/MEAs) gives an opportunity to overcome issues related to unsatisfactory high-temperature performance thanks to almost unlimited compositional space [5,6].

Low-density HEAs/MEAs (LDHEAs/LDMEAs) are one of the most prominent examples that highlight an advantage of multi-element alloying [7–9]. Having no strict definition, LDHEAs/LDMEAs are usually classified as the alloys with $\rho \leq 6\text{--}7 \text{ g/cm}^3$, and they can demonstrate unprecedented properties in a wide temperature interval. For instance, LDHEAs/LDMEAs, which contain Al, Ti, and a large portion of relatively lightweight refractory elements, surpass Ni- and TiAl-based alloys at $T = 22\text{--}1000^\circ\text{C}$ in specific (normalised to density) strength due to a structure dominated by intermetallic phases and a notable contribution of solid solution strengthening [6,10–14]. The same factors exert excellent strength retention capability at temperatures up to 1100 °C in other LDHEAs/LDMEAs, which consist of Al, Ti, and 3d elements, such as Cr, Fe, Ni, Co, Mn, Cu [15–20]. Besides high strength,

* Corresponding author at: World-Class Research Center “Advanced Digital Technologies”, State Marine Technical University, Saint Petersburg 198095, Russia
E-mail addresses: Yurchenko@ilwt.smtu.ru, yurchenko_nikita@bsu.edu.ru (N. Yurchenko).

<https://doi.org/10.1016/j.jalcom.2024.176445>

Received 26 July 2024; Received in revised form 26 August 2024; Accepted 9 September 2024

Available online 10 September 2024

0925-8388/© 2024 Elsevier B.V. All rights are reserved, including those for text and data mining, AI training, and similar technologies.

some of these alloys also show decent compressive plasticity at ambient and intermediate temperatures and outstanding oxidation resistance at 1000 °C owing to forming a protective Al₂O₃ oxide layer [18,19].

Meanwhile, the synthesis of LDHEAs/LDMEAs through a standard remelting process is accompanied by many difficulties. Properties of intermetallic-containing/based alloys, comprising a prevalent part of LDHEAs/LDMEAs, are highly sensitive to variations in the chemical composition [21,22]. Even small deviations that can occur during preparing raw metals and/or partial evaporation of the elements with low melting points induce scattering of the mechanical properties between different ingots, which is a major problem for potential applications of these alloys [22]. Besides, an inability to control the cooling temperature precisely initiates large residual stresses and/or formation of the intermetallic phases with undesirable morphology and inhomogeneous distribution, thereby degrading the overall performance of an alloy [22–25]. In this regard, powder metallurgy appears to be a more suitable way of obtaining LDHEAs/LDMEAs with a high content of intermetallic phases. Specifically, a combination of mechanical alloying (MA) and spark plasma sintering (SPS) provides almost porosity-free bulk specimens with a regular distribution of different phases, having nanometer sizes [26–30].

In our foregoing study, the LDMEA, consisting of inexpensive elements, namely Al, Cr, Fe, and Ti, was obtained by MA and SPS [31]. The equiatomic AlCrFeTi alloy was composed of a nano-grained (Fe, Ti)-rich C14 (hexagonal close packed, hcp) Laves matrix phase with homogeneously distributed Cr-rich bcc (body-centred cubic) and Al-rich L1₂ (an ordered version of face-centred cubic, fcc) nanoparticles. With such a structure and $\rho = 5.53 \text{ g/cm}^3$, the alloy achieved a specific yield strength of 258 MPa·cm³/g at 700 °C, outperforming all the reported as-cast refractory LDHEAs/LDMEAs, Ni-based Inconel 718 and TiAl-based alloys. However, one of the chief shortcomings of the alloy was its brittleness at $T < 700\text{--}800^\circ\text{C}$. Additional alloying is known to be an effective approach for improving the mechanical properties of as-cast LDHEAs/LDMEAs [19,20,32]. Meanwhile, the structure-property relationships of as-sintered LDHEAs/LDMEAs, as well as their response to heat treatment, are weakly established that require additional studies.

The main purposes of this study were to explore the possibilities of enhancing the mechanical performance of the prospective AlCrFeTi alloy through (i) adding Co, Ni, or Cu and (ii) further annealing. Co, Ni, or Cu were chosen as the elements that could increase the strength [33–38], while Cu could also improve the plasticity [37,38]. Following these suggestions, we synthesised the AlCrFeTiX ($X = \text{Co, Ni, Cu}$) alloys by MA and SPS and scrutinised their structure and mechanical properties in as-sintered and annealed conditions. Although these alloys were studied previously [39–43], and they showed promising oxidation [39, 40], corrosion [39], or wear [40,42,43] resistance, differences in the synthesis methods and the absence of high-temperature strength-plasticity characteristics, as well as information on the influence of heat treatment, are reasons for a more systematic investigation to evaluate the potential of such materials for structural applications.

2. Materials and methods

The commercial powders of Al (99.7 wt%, particle size < 30 μm), Cr (99.7 wt%, particle size in the range 10–30 μm), Fe (99.9 wt%, particle size < 75 μm), Ti (99.5 wt%, particle size < 45 μm), Co (99.8 wt%, particle size < 70 μm), Cu (99.97 wt%, particle size < 60 μm), Ni (99.9 wt%, particle size < 30 μm) were used as the precursors. 18 g batches of an stoichiometric Al:Cr:Fe:Ti:Co (1:1:1:1:1 mol), Al:Cr:Fe:Ti:Cu (1:1:1:1:1 mol), and Al:Cr:Fe:Ti:Ni (1:1:1:1:1 mol) mixtures were used for mechanical alloying at 694 rpm (jar rotated at 1388 rpm) for 60 min in a water-cooling double-station planetary ball mill (Activator 2S, Activator, Russia), which is high energy planetary ball mill and allows reaching centrifugal acceleration more than 90 g [44]. The milling ball (stainless steel, 6 mm diameter) to powder mixtures weight ratio was 20:1. Before the milling, a stainless steel jar of 250 ml capacity

was vacuumed, filled with the 99.98 %-purity argon having a pressure of 4 atm and then sealed. It is critical to note that the powders became pyrophoric, that is fresh as-milled powders could self-ignite after opening the jars. The powders were unloaded from jars and loaded to graphite die for SPS in a glove box in an argon atmosphere.

Cylindrical graphite die (the inner diameter of 30 mm) was filled with a desired amount of the mixed powders. Then, the powders were consolidated using a SPS apparatus (Labox 650, Sinter Land, Japan) using the following parameters: heated in vacuum (15–20 Pa) at the rate of 100 °C/min, the temperature of 900 °C, under uniaxial loading of 50 MPa, and dwell time of 10 min. After sintering, the specimens were free cooled in vacuum; cooling time to room temperature was ~15 min. Disc-shaped samples of 30 mm in diameter and 7 mm thick were obtained.

The specimens measured $3 \times 3 \times 5 \text{ mm}^3$ were cut from the disc-shaped samples after SPS using electrical discharge machining. A part of the specimens were annealed at 1000 °C for 24 h with further air cooling. Prior to annealing, the specimens were sealed in a vacuumed (10^{-2} torr) quartz tube filled with titanium chips to prevent oxidation. The specimens after SPS and annealing were used for structural investigations and mechanical properties evaluation.

Microstructural investigations were performed using X-ray diffraction (XRD, Rigaku Ultima IV), scanning electron microscopy (SEM; FEI Quanta 600 FEG or Tescan Mira3) and transmission electron microscopy (TEM; JEM JEOL-2100) together with energy-dispersive X-ray spectroscopy (EDS, SEM: EDAX Octane Elect Plus (FEI Quanta 600 FEG) or Ultim Max 65 (Tescan Mira3); TEM: INCA x-sight). Samples for XRD and SEM analysis were prepared by careful mechanical polishing to mirror surfaces using Buehler MasterMet 2 Suspension. For TEM examinations, thin foils were prepared using a Tenupol-5 twin-jet electro-polisher with an electrolyte containing a mixture of 600 ml of methanol, 360 ml of butanol, and 60 ml of perchloric acid at -35°C and 29.5 V. Selected area electron diffraction (SAED) patterns were used for phase identification. The volume fractions and dimensions of different phases were measured by using a Digimizer Image Analysis Software or ImageJ. The actual chemical compositions of the alloys after SPS (measured SEM-EDS; the scan area was $\sim 1 \times 1 \text{ mm}^2$) are presented in Table 1.

The densities of the alloys were determined using hydrostatic weighing (Archimedes' principle) of three samples measured $3 \times 3 \times 5 \text{ mm}^3$. The measured densities of the AlCrFeTiCo, AlCrFeTiCu, and AlCrFeTiNi alloys after SPS were 5.91 ± 0.03 , 5.93 ± 0.05 , and $5.86 \pm 0.02 \text{ g/cm}^3$, respectively.

Vickers microhardness tests were conducted at room temperature using 300 g load. At least 10 measurements per each data point were made.

Isothermal compression tests of rectangular specimens measured $3 \times 3 \times 5 \text{ mm}^3$ were carried out at 25 and 600 °C using an Instron 300LX machine equipped with a radial furnace. At 600 °C, the specimens were placed into the preheated furnace and held for ~10 min to equilibrate the temperature before testing. The temperature was controlled by a thermocouple attached to a side surface of the specimen. The initial strain rate was 10^{-4} s^{-1} .

Table 1
Actual chemical compositions of the AlCrFeTiX ($X = \text{Co, Cu, Ni}$) alloys after SPS.

Alloy	Chemical composition, at%						
	Al	Cr	Fe	Ti	Co	Cu	Ni
AlCrFeTiCo	19.1 ± 0.5	20.3 ± 0.5	21.3 ± 0.8	19.8 ± 1.0	19.6 ± 0.4	-	-
AlCrFeTiCu	20.1 ± 0.3	19.8 ± 0.4	20.2 ± 0.6	18.8 ± 0.1	-	21.1 ± 0.6	-
AlCrFeTiNi	19.4 ± 0.9	20.6 ± 0.7	21.3 ± 0.2	19.7 ± 0.7	-	-	19.1 ± 0.3

3. Results

3.1. Structure after SPS

The structure of the alloys after SPS was firstly studied by SEM (Fig. 1 (a-c)). In all the alloys, a three-phase structure was formed,

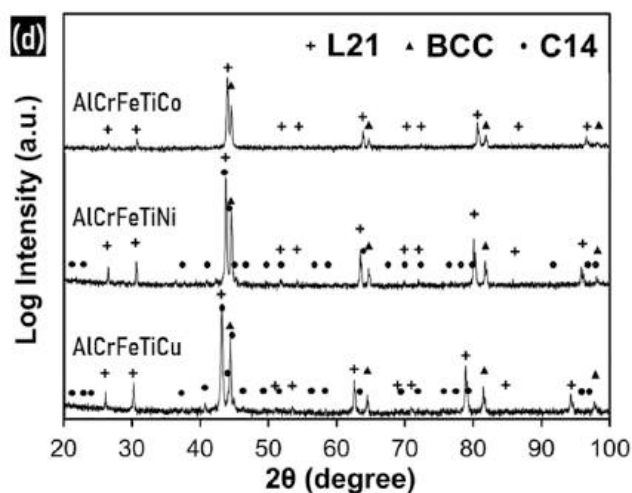
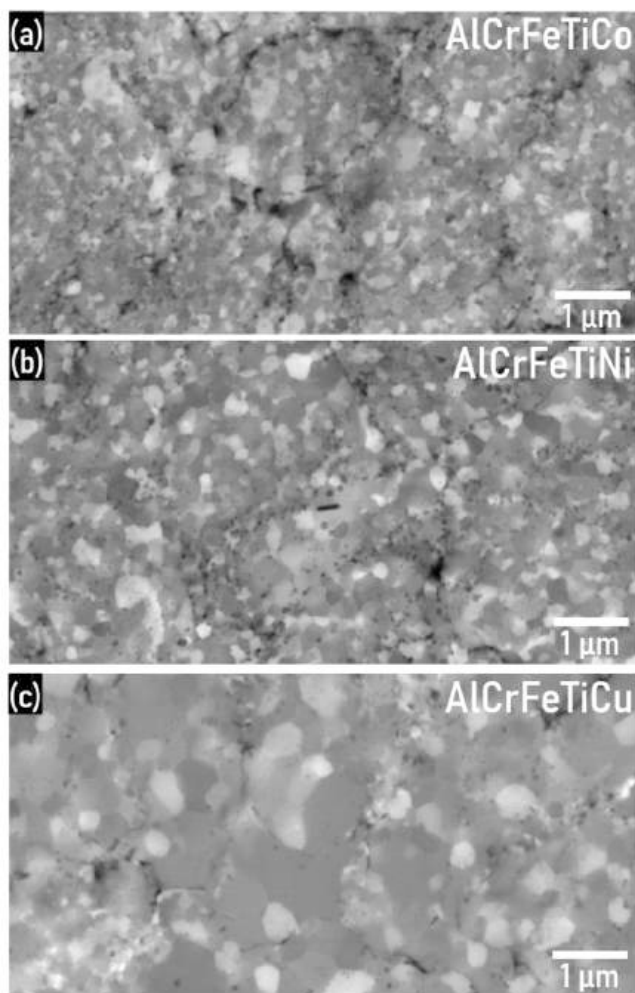


Fig. 1. Characterisation of the structure of the AlCrFeTiCo, AlCrFeTiNi, and AlCrFeTiCu alloys after SPS: (a-c) - SEM-BSE images of the typical structures of the AlCrFeTiCo (a), AlCrFeTiNi (b), and AlCrFeTiCu (c) alloys; (d) - diffraction patterns with identified phases.

differentiated by a size of structural constituents, which were finer in the AlCrFeTiCo and AlCrFeTiNi alloys (Fig. 1(a, b)). According to SEM-BSE images, a dark-grey matrix contained relatively large and homogeneously distributed light-grey particles/grains. The third phase was presented by highly dispersed dark particles, which appeared both as individual particles inside the dark-grey matrix or as discontinuous networks surrounding the areas containing dark-grey matrix and light-grey particles/grains. According to XRD analysis (Fig. 1(d)), all the alloys consisted of the main Heusler (L2₁) phase, as judging from the highest relative intensity of the Bragg's peaks. In the AlCrFeTiCo alloy, an additional bcc phase was observed, whilst the AlCrFeTiNi and AlCrFeTiCu alloys contained two extra phases: bcc and C14 Laves phases. The lattice parameters of the corresponding phases were similar amid the alloys studied (Table 2).

A more detailed study of the structure of the AlCoCrFeTi and AlCrFeNiTi alloys was performed by TEM (Fig. 2). Analysis of SAED patterns revealed a mixture of the L2₁, bcc, and C14 Laves phases in both alloys. The L2₁ and bcc phases prevailed in the structure, and they had close average grain/particle sizes of 120 or 230 nm in the AlCoCrFeTi or AlCrFeNiTi alloy, respectively. In turn, the C14 Laves phase appeared as individual precipitates within or adjacent to L2₁/bcc grains/particles. The average sizes of these precipitates were 40 and 70 nm in the AlCoCrFeTi and AlCrFeNiTi alloy, respectively. Both diffuse boundaries and a complex contrast inside some grains/particles should be noted that could indicate significant internal stresses. The inability to detect the C14 Laves phase in the AlCoCrFeTi alloy by XRD analysis could be attributed to the low volume fraction (< 5 %) of this phase.

TEM-EDS analysis showed that the constituent phases had complex chemical compositions (Table 3). In the AlCoCrFeTi alloy, the L2₁ phase was enriched in Al and Co, and it contained a nominal amount of Ti and Fe, while depleted with Cr. In the AlCrFeNiTi alloy, the L2₁ phase was also lean in Cr, yet rich in Ni and Ti, as well as containing nominal concentrations of Al and Fe. In turn, the bcc and the C14 Laves phases of both alloys were enriched with Cr and contained nominal concentrations of Fe, while the ratios between the other elements were similar (Table 2).

3.2. Structure after annealing

Microstructural changes induced by annealing were tracked by SEM (Fig. 3(a-c)). All three alloys experienced coarsening of structural constituents. The microstructures of the AlCrFeTiCo and AlCrFeTiNi alloys appeared to be close to each other (Fig. 3(a, b)). According to SEM-BSE images, the dark-grey matrix phase contained homogeneously distributed light-grey and dark particles. The volume fractions of the matrix phase were 59 and 70 % in the AlCrFeTiCo and AlCrFeTiNi alloys, respectively. The volume fractions of light-grey particles were 30 and 20 % in the AlCrFeTiCo and AlCrFeTiNi alloys, respectively. Lastly, the volume fractions of dark particles were 11 and 10 % in the AlCrFeTiCo and AlCrFeTiNi alloys, respectively. In the AlCrFeTiCu alloy (Fig. 3(c)), annealing led to a rapid coarsening of the dark-grey matrix (57 %), in which embedded large light-grey (40 %) and tiny dark (3 %) particles. XRD analysis revealed no difference in the phase composition of the alloys compared to the as-sintered state (Fig. 3(d)). In the diffraction

Table 2

Lattice parameters of the corresponding phases of the AlCrFeTiCo, AlCrFeTiNi and AlCrFeTiCu alloys after SPS.

Alloy	Lattice parameter, nm		
	L2 ₁ phase	bcc phase	C14 Laves phase
AlCrFeTiCo	0.5836 ± 0.0003	0.2883 ± 0.0004	-
AlCrFeTiNi	0.5867 ± 0.0004	0.2884 ± 0.0002	a = 0.4858 ± 0.0002, c = 0.7793 ± 0.0005
AlCrFeTiCu	0.5942 ± 0.0005	0.2892 ± 0.0003	a = 0.4815 ± 0.0003, c = 0.7723 ± 0.0003

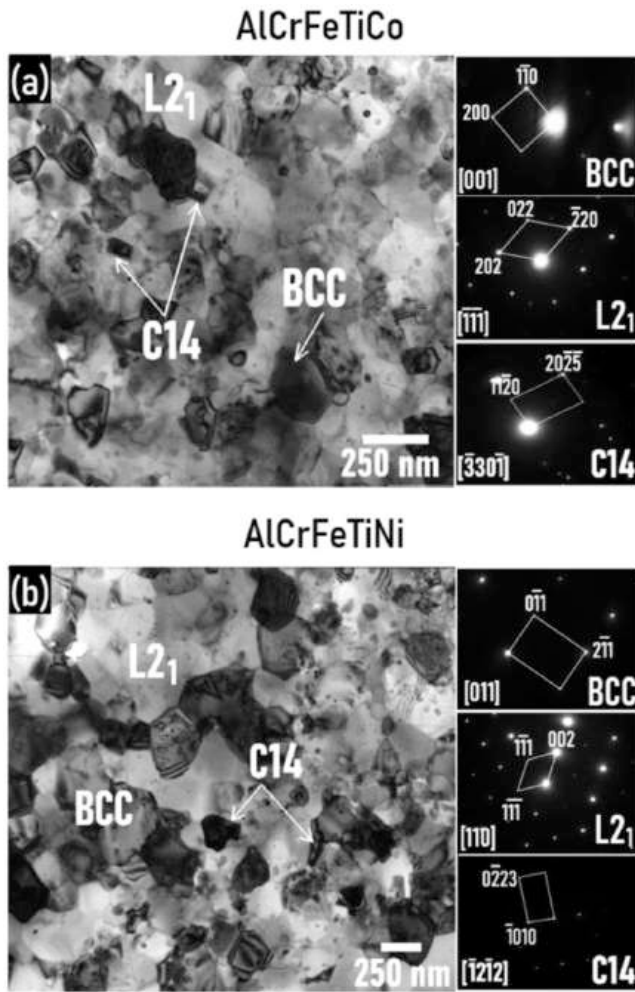


Fig. 2. Detailed characterisation of the structure of the AlCrFeTiCo (a) and AlCrFeTiNi (b) alloys after SPS: TEM bright-field images and SAED patterns of the corresponding phases.

Table 3

Chemical compositions of the corresponding phases of the AlCrFeTiCo and AlCrFeTiNi alloys after SPS. Data were collected using TEM-EDS.

Elements, at %	Al	Cr	Fe	Ti	Co	Ni
Phase	AlCrFeTiCo					
L2 ₁	30.3 ± 0.8	3.8 ± 0.7	19.3 ± 1.2	21.7 ± 1.4	24.9 ± 1.3	-
bcc	7.3 ± 1.6	64.7 ± 5.7	20.1 ± 0.5	4.8 ± 1.1	3.2 ± 1.2	-
C14 Laves	14.0 ± 3.0	34.9 ± 2.5	18.2 ± 0.9	20.3 ± 2.1	12.6 ± 1.4	-
Phase	AlCrFeTiNi					
L2 ₁	20.3 ± 1.5	4.5 ± 0.5	21.4 ± 0.7	26.6 ± 1.8	-	27.2 ± 1.4
bcc	5.9 ± 0.5	65.4 ± 1.8	20.3 ± 0.6	5.4 ± 1.3	-	2.9 ± 1.2
C14 Laves	11.5 ± 3.5	32.9 ± 2.8	17.4 ± 0.5	25.2 ± 3.2	-	13.0 ± 1.0

pattern of the AlCrFeTiCo alloy, only the L2₁ and bcc phases were detected, while the AlCrFeTiNi and AlCrFeTiCu alloys consisted of the L2₁, bcc, and C14 Laves phases. No noticeable variations in the lattice parameters of the corresponding phases as a result of annealing were also observed (Table 4).

Detailed analysis of the structure after annealing was performed by

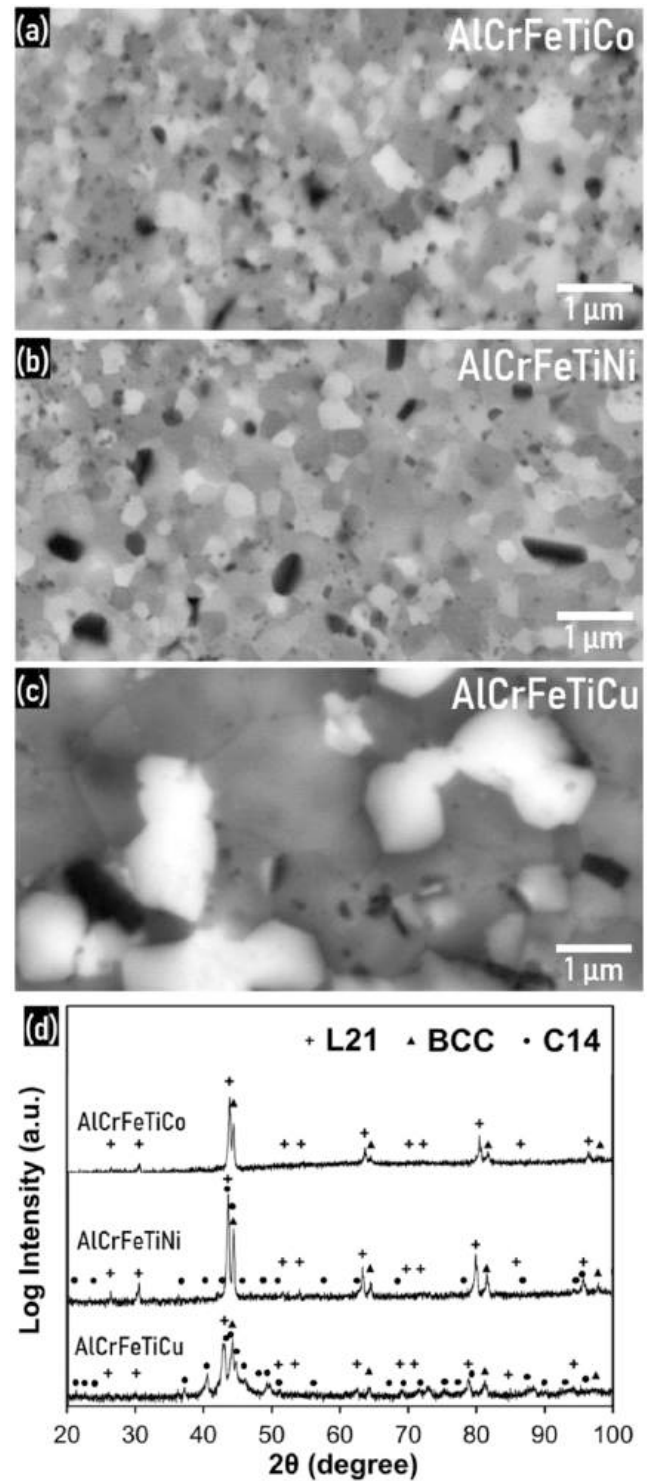


Fig. 3. Characterisation of the structure of the AlCrFeTiCo, AlCrFeTiNi, and AlCrFeTiCu alloys after annealing: (a-c) - SEM-BSE images of the typical structures of the AlCrFeTiCo (a), AlCrFeTiNi (b), and AlCrFeTiCu (c) alloys; (d) - diffraction patterns with identified phases.

TEM (Fig. 4). Bright-field images supplied with SAED patterns confirmed the three-phase structure in all the alloys studied. In the AlCrFeTiCo and AlCrFeTiNi alloys (Fig. 4(a, b)), the arrangements of the L2₁, bcc, and C14 Laves phases, as well as their form (grains/particles for the L2₁ and bcc phases, and precipitates for the C14 Laves phase), resembled those of the as-sintered state (Fig. 2). However, the sizes of these structural constituents increased. In the AlCrFeTiCo alloy, the

Table 4

Lattice parameters of the corresponding phases of the AlCrFeTiCo, AlCrFeTiNi and AlCrFeTiCu alloys after annealing.

Alloy	Lattice parameter, nm		
	L2 ₁ phase	bcc phase	C14 Laves phase
AlCrFeTiCo	0.5842 ± 0.0003	0.2885 ± 0.0004	-
AlCrFeTiNi	0.5876 ± 0.0004	0.2884 ± 0.0002	a = 0.4891 ± 0.0006, c = 0.7939 ± 0.0011
AlCrFeTiCu	0.5943 ± 0.0003	0.2898 ± 0.0003	a = 0.4832 ± 0.0005, c = 0.7907 ± 0.0013

average size of the L2₁/bcc grains/particles and C14 Laves precipitates enlarged to 400 nm and 115 nm, respectively (Fig. 4(a)). In the AlCrFeTiNi alloy, the L2₁/bcc grains/particles and C14 Laves precipitates were estimated to be 300 nm and 125 nm, respectively (Fig. 4(b)). Compared to the as-sintered state, the boundaries, as well as the interiors, of structural constituents became clearer after annealing, indicating the decreased internal stresses.

Somewhat alterations in the content of constitutive elements in the L2₁ and C14 Laves phases should be noted (Table 5). In the AlCrFeTiCo alloy, the L2₁ phase became leaner in Al and slightly richer in Cr and Fe, while the C14 Laves phase of the AlCrFeTiNi alloy appeared to be more abundant in Cr and Fe and poorer in Ti and Ni. Meanwhile, the chemical composition of the bcc phases in the AlCrFeTiCo and AlCrFeTiNi alloys remained unaffected by annealing (Table 5).

The coarsest L2₁, bcc, and C14 Laves phases were found in the AlCrFeTiCu alloy (Fig. 4(c)). The size of these structural constituents exceeded 1 μm (in certain directions). The C14 Laves phase precipitates often had a needle-like form. TEM-EDS analysis showed that the chemical composition of the L2₁ phase was close (in terms of the ratios of main Al, Cr, Fe, and Ti elements) to that of the AlCrFeTiCo and AlCrFeTiNi alloys (Table 5). Meanwhile, the bcc phase contained an approximately twice lower Cr content, and the C14 Laves phase was leaner in Cr and richer in Al, compared to the same phases found in the AlCrFeTiCo and AlCrFeTiNi alloys.

3.3. Mechanical properties after SPS and annealing

Mechanical properties of the alloys were evaluated firstly by microhardness measurements. Microhardness of the AlCrFeTiCo, AlCrFeTiNi, or AlCrFeTiCu alloy after SPS was 1009, 867, or 710 HV, respectively. Microhardness dropped after annealing, and the annealing-induced decrease in microhardness was minor (< 10 %) in the AlCrFeTiCo and AlCrFeTiNi alloys, but it was noticeable (> 30 %) in the AlCrFeTiCu alloy (Fig. 5).

Further, we performed compression tests of the alloys after SPS and after annealing at 25 and 600 °C. Fig. 6 and Table 6 collect the engineering stress-strain curves and mechanical properties (yield strength (σ_{YS}), peak strength (σ_m), and plastic strain (ε)), respectively. At 25 °C, all the alloys after SPS were brittle and fractured in the elastic region (Fig. 6(a)). The AlCrFeTiCo alloy showed σ_m = 3792 MPa, while the AlCrFeTiNi and AlCrFeTiCu alloys fractured at σ_m ≈ 2300 MPa (Fig. 6(a), Table 6). At 600 °C, the AlCrFeTiCo alloy demonstrated the best performance: σ_{YS} = 1960 MPa, σ_m = 2121 MPa, and ε = 1.8 % (Fig. 6(b), Table 6). The AlCrFeTiCu alloy also showed signatures of plasticity (ε = 1 %) accompanied by a prominent strength reduction (σ_{YS} = 780 MPa; σ_m = 952 MPa). The AlCrFeTiNi alloy remained brittle and fractured at σ_m = 742 MPa (Fig. 6(b), Table 6).

Annealing did not improve the room-temperature properties of the alloys studied (Fig. 6(c), Table 6). All the alloys after annealing were brittle at 25 °C, and their σ_m values varied from as high as 3244 MPa (the AlCrFeTiNi alloy) to as low as 1170 MPa (the AlCrFeTiCu alloy) (Fig. 6(c), Table 6). Nevertheless, annealing enhanced the mechanical properties at 600 °C, and the most prominent response was observed in the AlCrFeTiCo and AlCrFeTiNi alloys (Fig. 6(d), Table 6). Specifically, the

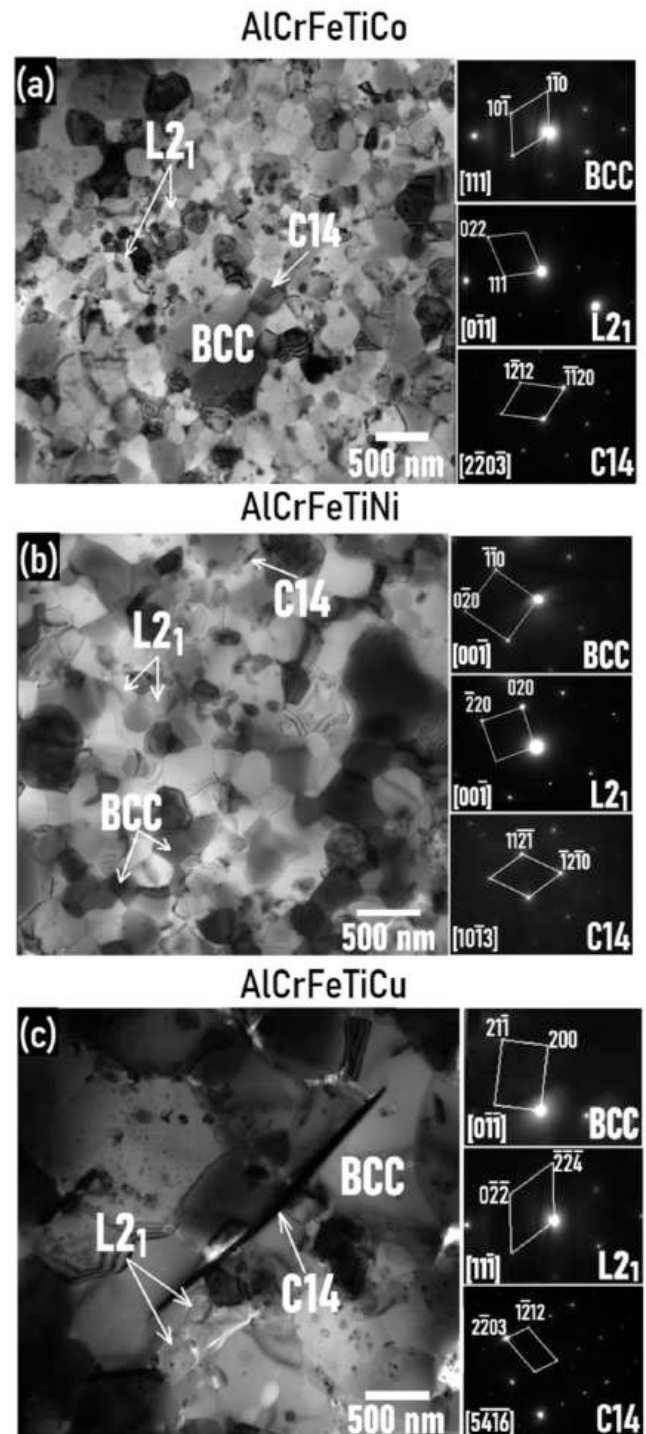


Fig. 4. Detailed characterisation of the structure of the AlCrFeTiCo (a), AlCrFeTiNi (b), and AlCrFeTiCu (c) alloys after annealing: TEM bright-field images and SAED patterns of the corresponding phases.

AlCrFeTiCo alloy showed a 15 %-increase in strength (σ_{YS} = 2264 MPa), pronounced strengthening up to σ_m = 2692 MPa, and more than 2.5 times higher compressive plasticity (ε = 4.7 %) with an extended steady flow stage, as compared to the as-sintered state (Fig. 6(b), Table 6). The AlCrFeTiNi alloy became more ductile (ε = 1 %) and stronger (σ_{YS} = 2200 MPa). For the AlCrFeTiCu alloy, the annealing had a neutral or even negative effect that resulted in a subtle increase in σ_{YS} up to 818 MPa and reduction of ε down to 0.2 % (Fig. 6(d), Table 6).

Table 5

Chemical compositions of the corresponding phases of the AlCrFeTiCo, AlCrFeTiNi and AlCrFeTiCu alloys after annealing. Data were collected using TEM-EDS.

Elements, at%	Al	Cr	Fe	Ti	Co	Ni	Cu
AlCrFeTiCo							
L ₂₁	23.0 ± 1.5	6.4 ± 0.7	22.3 ± 1.1	23.4 ± 2.0	25.0 ± 0.9	-	-
bcc	5.6 ± 0.3	67.9 ± 1.6	19.9 ± 1.4	3.8 ± 0.4	2.8 ± 0.2	-	-
C14 Laves	15.4 ± 1.3	37.7 ± 2.1	20.7 ± 0.8	13.0 ± 0.3	13.2 ± 0.5	-	-
AlCrFeTiNi							
L ₂₁	24.2 ± 1.8	4.2 ± 0.4	20.2 ± 0.6	24.8 ± 1.2	-	26.6 ± 1.3	-
bcc	5.2 ± 0.8	69.0 ± 1.1	20.2 ± 0.9	3.4 ± 0.2	-	2.1 ± 0.4	-
C14 Laves	14.5 ± 0.4	41.2 ± 1.4	20.2 ± 0.7	16.4 ± 0.5	-	7.8 ± 0.6	-
AlCrFeTiCu							
L ₂₁	27.1 ± 1.0	6.2 ± 0.4	21.5 ± 1.1	20.9 ± 0.9	-	-	24.4 ± 0.5
bcc	21.8 ± 0.7	37.2 ± 3.4	13.6 ± 0.6	12.1 ± 2.1	-	-	15.3 ± 1.7
C14 Laves	21.4 ± 1.6	25.6 ± 2.3	20.8 ± 1.2	17.9 ± 0.3	-	-	14.3 ± 0.9

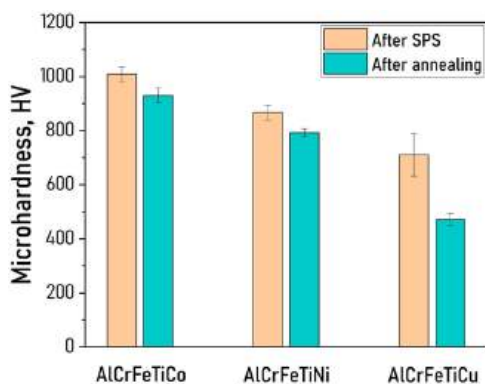


Fig. 5. Microhardness of the AlCrFeTiCo, AlCrFeTiNi, and AlCrFeTiCu alloys after SPS and after annealing.

4. Discussion

4.1. Structure

The alloys studied are modifications of the AlCrFeTi LDMEA, so a comparison of the structures should be presented. We found that additions of Co, Ni, and Cu to the AlCrFeTi alloy altered its phase structure. Instead of the C14 Laves matrix phase with the embedded bcc and L₁₂ particles observed in the AlCrFeTi alloy [31], the L₂₁ matrix phase containing the bcc and C14 Laves phase precipitates formed in the AlCrFeTiX (x = Co, Ni, Cu) alloys. Such a transformation of the phase structure upon alloying can be analysed using a CALPHAD (CALCULATION of PHase Diagrams) method (Fig. 7).

According to thermodynamic modelling, the formation of a multi-phase structure is expected in all the alloys. In the AlCrFeTiCo alloy, the solidification starts from a (Co, Al)-rich B2 (an ordered version of bcc) phase, with subsequent appearance of a (Cr, Ti)-rich C14 Laves phase and a Cr-rich bcc phase (Fig. 7(a)). The AlCrFeTiNi alloy crystallises through the Cr-rich bcc phase, which is followed by forming a palette of phases, such as (Fe, Al)-rich and (Ni, Al)-rich B2 phases, a (Ni, Ti, Al)-rich L₂₁ phase, and a (Fe, Ti)-rich C14 Laves phase (Fig. 7(b)). For the AlCrFeTiCu alloy, CALPHAD predicts the primary solidification of the Cr-rich bcc phase and subsequent nucleating the (Fe, Ti)-rich C14 Laves

phase, a (Cu, Al)-rich bcc phase, and a Cu-rich fcc phase (Fig. 7(c)).

The experimental and predicted structures of the AlCrFeTiX (x = Co, Ni, Cu) alloys are in a partial agreement. Thermodynamic modelling correctly foresees forming the bcc and C14 Laves phases. Moreover, the modelled chemical compositions of the bcc phases coincide well with the experimental ones. However, CALPHAD cannot predict the L₂₁ phase, which is expected only in the AlCrFeTiNi alloy. Another controversial point is the melting point, T_m, of the AlCrFeTiCu alloy, which is prognosticated to be 1007 °C. Evidently, CALPHAD underestimates the T_m of the AlCrFeTiCu alloy, since no signatures of melting were found after annealing at 1000 °C. The inconsistencies found between the experimental and calculated data can be ascribed to imperfections of the current databases [45].

Since forming the L₂₁ phase in the alloys studied was triggered by the additions of Co, Ni, or Cu, we delved into corresponding phase diagrams. In ternary Co-Ti-Al [46], Ni-Ti-Al [47], and Cu-Ti-Al [48] systems, the respective Co₂TiAl, Ni₂TiAl, and Cu₂TiAl L₂₁ phases were experimentally observed. In the alloys studied, however, the L₂₁ phase had a more complex chemical composition. EDS analysis of the AlCrFeTiCo and AlCrFeTiNi alloys after SPS showed that the concentrations of Co and Ni did not exceed ~ 25 at%, which were a half of that of required to create a X₂TiAl L₂₁ phase. We infer that the deficit of Co and Ni atoms could be compensated by Fe and Cr, which are prone to occupy the same X-element sublattice [49–51]. However, even in the case of such an elemental partitioning, deviations from an ideal X₂TiAl stoichiometry still existed. Specifically, in the AlCrFeTiCo alloy, the L₂₁ phase contained 52 at% of Ti and Al in sum, while, in the AlCrFeTiNi alloy, this phase was richer in the X-elements, with a total amount of Ni, Fe, and Cr equal to ~ 53 at%. These deviations in stoichiometry can partly explain differences in mechanical properties that will be discussed in the next section.

Some comments should also be given for the thermal stability of the AlCrFeTiX (x = Co, Ni, Cu) alloys. Annealing at 1000 °C resulted in (i) a coarsening of the L₂₁/bcc grains/particles and C14 Laves precipitates and (ii) alterations of the chemical composition of certain phases. Specifically, the annealing equilibrated the content of Al and Ti in the L₂₁ phase of the AlCrFeTiCo and AlCrFeTiNi alloys, making the ratio of Ti:Al ≈ 1:1, which corresponded to that of the ideal X₂TiAl. Meanwhile, the annealing-induced coarsening could be driven by a high density of grain/interphase boundaries, similar to the AlCrFeTi LDMEA [31]. Yet, unlike the AlCrFeTi alloy, which experienced a minor increase in the size of structural constituents, the AlCrFeTiX (x = Co, Ni, Cu) alloys coarsened by 2–3 times. Nevertheless, the AlCrFeTiCo and AlCrFeTiNi alloys preserved the nano-sized structure, while, in the AlCrFeTiCu alloy, the dimensions of the phases went beyond 1 μm. The higher coarsening rate can be connected with a lower T_m (Fig. 7) of the alloys studied compared to the AlCrFeTi counterpart [31]. This assumption, despite some uncertainties in the CALPHAD predictions of T_m, can also rationalise a much coarser structure observed in the AlCrFeTiCu alloy both after SPS and annealing.

4.2. Mechanical properties

Alterations in the phase structure with the additions of Co, Ni, or Cu were positive for the mechanical properties of the AlCrFeTi LDMEA. Forming the L₂₁ matrix phase instead of the C14 Laves phase maintained high hardness, which exceeded 1000 HV in the AlCrFeTiCo alloy after SPS, and provided better performance during compression. Despite the retaining of room-temperature brittleness, the AlCrFeTiX (x = Co, Ni, Cu) alloys after SPS reached 2–3 times higher peak strength values compared to the AlCrFeTi LDMEA. Also, the AlCrFeTiCo alloy after SPS manifested signatures of plasticity already at 600 °C, while the AlCrFeTi alloy remained brittle up to 800 °C. The latter observation could be connected with: (i) alleviated plastic deformation mediated by dislocation motion due to thermal activation induced by a reduced T_m [52] and (ii) dominating L₂₁ phase, which appears to be more deformable than

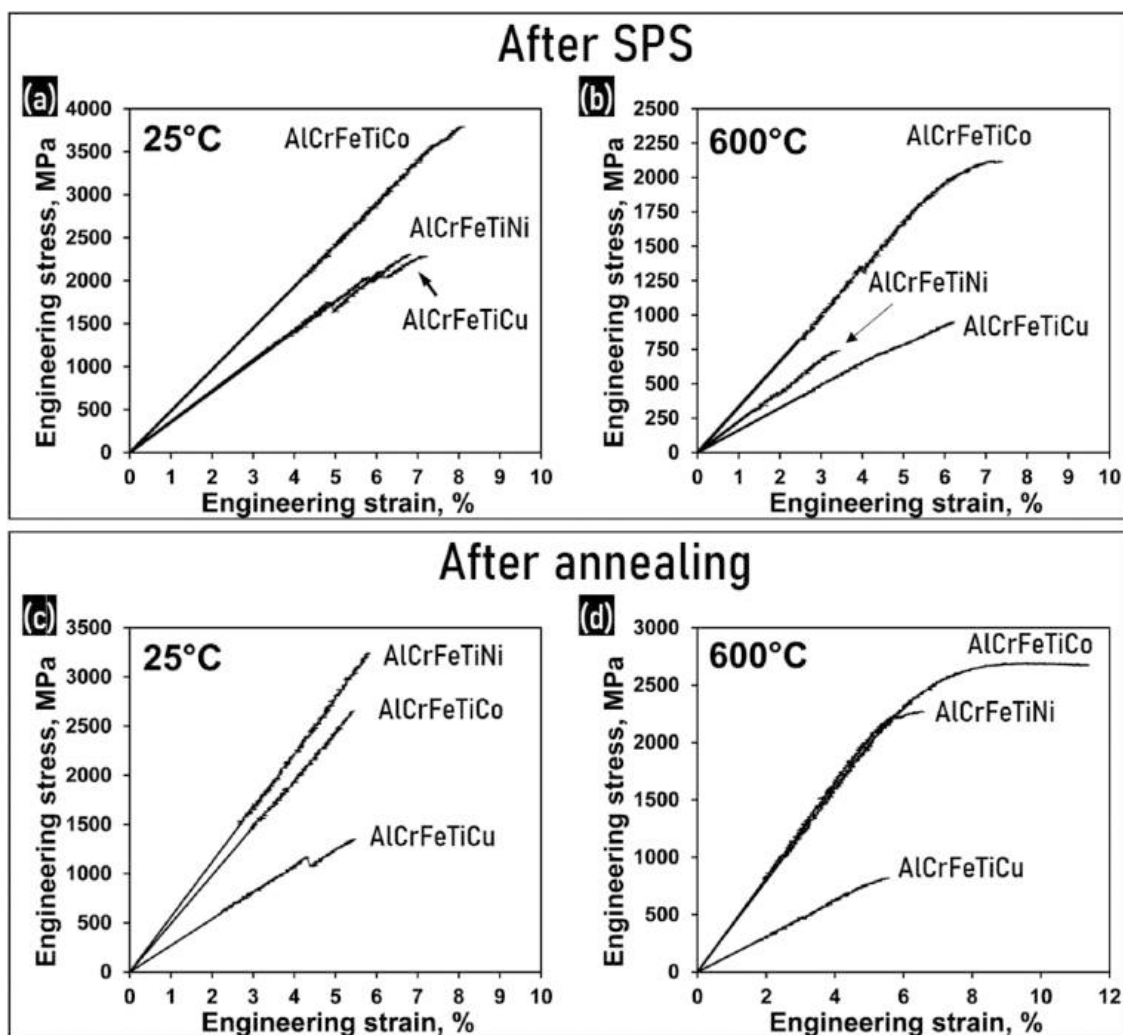


Fig. 6. Engineering stress-strain curves of the AlCrFeTiCo, AlCrFeTiNi, and AlCrFeTiCu alloys after SPS (a, b) and after annealing (c, d) obtained during the compression tests at 25 (a, c) and 600 °C (b, d).

Table 6

Mechanical properties (yield strength (σ_{YS}), peak strength (σ_m), and plastic strain (ϵ)) of the AlCrFeTiCo, AlCrFeTiNi, and AlCrFeTiCu alloys after SPS and after annealing obtained during compression tests at 25 and 600 °C.

Alloy	Temperature, °C	State	σ_{YS} , MPa	σ_m , MPa	ϵ , %
AlCrFeTiCo	25	after SPS	-	3792	0
	600	after SPS	1960	2121	1.8
AlCrFeTiCo	25	after annealing	-	2652	0
	600	after annealing	2264	2692	4.7
AlCrFeTiNi	25	after SPS	-	2308	0
	600	after SPS	-	742	0
AlCrFeTiNi	25	after annealing	-	3244	0
	600	after annealing	2200	2274	1
AlCrFeTiCu	25	after SPS	-	2278	0
	600	after SPS	780	952	0.4
AlCrFeTiCu	25	after annealing	-	1170	0
	600	after annealing	818	818	0.2

the C14 Laves phase [53].

Meanwhile, the effect of annealing on the mechanical properties of the AlCrFeTiX ($x = \text{Co, Ni, Cu}$) alloys was complex. Specifically, the annealing decreased the hardness (possibly due to lowering of internal stresses) and could not eliminate room-temperature brittleness, while improving compressive properties of the AlCrFeTiCo and AlCrFeTiNi alloys at 600 °C. Both alloys became stronger and more ductile at this

temperature. In the AlCrFeTiCo alloy, annealing led to a 15 %-increase in strength and more than a twofold increase in plastic strain. The increase in plasticity was accompanied by the appearance of an extended steady flow stage, indicating the pronounced dislocation activity. In turn, the AlCrFeTiCu alloy showed a negative response to the annealing, which included 30 %-decrease in hardness and halved plasticity at 600 °C.

Since the phase composition of the alloys studied remained constant, such a complex effect of annealing on the properties could be connected with (i) the coarsening and (ii) chemical composition alterations. The AlCrFeTiCu alloy experienced the most pronounced increase ($> 1 \mu\text{m}$) in the size of structural constituents that led to an inevitable decrease in grain boundary strengthening - one the major sources for the strength of the materials obtained by SPS [54–56]. Reduced plasticity of the AlCrFeTiCu alloy can also be reasoned by coarsening. For intermetallics, the grain size is among the crucial parameters that govern their plasticity [57]. A transition from nano- to micron-sized structure embrittles the intermetallic compound and vice versa [58,59].

Although the AlCrFeTiCo and AlCrFeTiNi alloys were amenable to somewhat coarsening, the strength loss due to weakening of grain boundary strengthening effect could be overcome by the equilibrating the content of Ti and Al in the L₂₁ matrix phase. The properties of many intermetallics are sensitive to the degree of ordering [60] affecting the antiphase boundary (APB) energy [61], which are, in turn, dependent on the chemical composition. In some cases, the compounds having

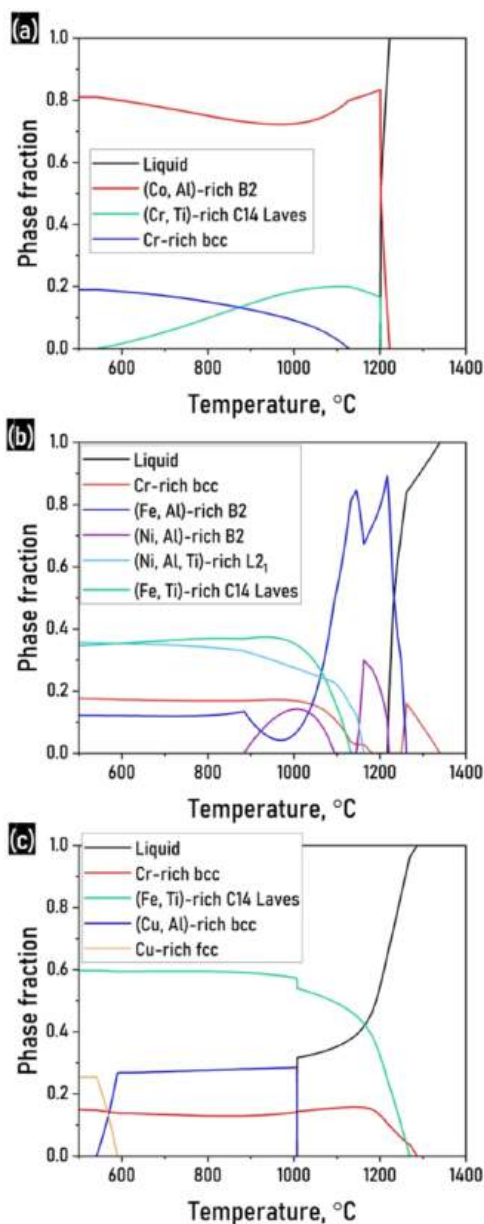


Fig. 7. Calculated temperature dependence of equilibrium phases of the AlCrFeTiCo (a), AlCrFeTiNi (b), and AlCrFeTiCu (c) alloys. The CALPHAD was realised with a Thermo-Calc (version 2022b) software and a TCHEA5 (high-entropy alloys) database.

stoichiometric (or nearly stoichiometric) composition, which indicates the maximum degree of ordering and APB energy, show higher strength and/or plasticity compared to off-stoichiometric counterparts due to specific dislocation configurations and their interactions. Albeit the estimation of the degree of ordering in such chemically complex systems as HEAs is known to be a non-trivial task [32,62–64], we, nevertheless, suggest that all the features mentioned above for “conventional” intermetallics could be responsible for the improvement of the mechanical performance of the AlCrFeTiCo and AlCrFeTiNi alloys after annealing.

Lastly, we must note that the AlCrFeTiCo and AlCrFeTiNi alloys after annealing showed exceptionally high yield strength values at 600 °C, which were 2064 and 2200 MPa, respectively. To understand the status quo of these values, we normalised them to density (specific yield strength (SYS) and compared with those of other LDMEAs/LDHEAs available in literature [10–12,15–19,32,34,65–69] (Fig. 8). The dataset contained 33 LDMEAs/LDHEAs having different phase compositions,

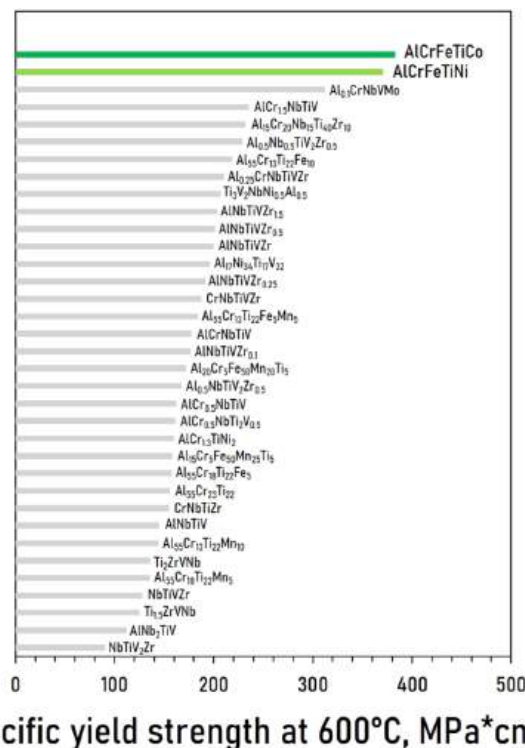


Fig. 8. Specific yield strength (SYS) of the AlCrFeTiCo and AlCrFeTiNi alloys after annealing and other LDMEAs/LDHEAs at 600 °C [10–12,15–19,32,34,65–69].

which were dominated by a palette of intermetallics, like B2, C14/C15 Laves phases, L1₂, C11_b, and, particularly, L2₁ phase. The AlCrFeTiCo and AlCrFeTiNi alloys with respective SYS values of 383 and 371 MPa*cm³/g outperformed all the alloys from the dataset. The most closest SYS = 312 MPa*cm³/g was shown by the Al_{0.1}CrNbVMo alloy with a structure consisting of bcc matrix phase and alumina inclusions obtained by MA and SPS [55]. Meanwhile, SYS of the other LDMEAs/LDHEAs synthesised by casting methods did not exceed 250 MPa*cm³/g. Among them, the most high-strength AlCr_{1.5}NbTiV alloy with a structure comprised a B2 matrix and blocky C14 Laves phase particles achieved only 231 MPa*cm³/g [11].

As was mentioned above, the record-high SYS values of the AlCrFeTiCo and AlCrFeTiNi alloys could stem from the synergistic effects from grain boundary strengthening and dominance of intermetallic phases in the structure. Although evading the room-temperature brittleness remained an issue yet to be solved, good oxidation, corrosion, and wear resistance, together with outstanding specific strength, make the AlCrFeTiCo and AlCrFeTiNi alloys very attractive materials that can withstand in-service high-temperature compressive loads.

5. Conclusions

In this study, the structure and mechanical properties of the low-density (< 6 g/cm³) AlCrFeTiX (x = Co, Ni, Cu) high-entropy alloys after SPS and annealing at 1000 °C for 24 h were reported. The following conclusions could be drawn:

- 1) Both after SPS and annealing, the AlCrFeTiX (x = Co, Ni, Cu) alloys had a similar phase structure consisting of the L2₁ matrix phase with homogeneously distributed bcc and C14 Laves phase precipitates. The L2₁ matrix phase was enriched with Fe, Ti, Al, and the corresponding element of Co, Ni, or Cu. In the bcc and C14 Laves phases of all the alloys, Cr prevailed. All the alloys had a nano-sized structure

after SPS that retained in the AlCrFeTiCo and AlCrFeTiNi alloys after annealing, while it became micron-sized in the AlCrFeTiCu alloy.

- After SPS, microhardness of the AlCrFeTiCo, AlCrFeTiNi, or AlCrFeTiCu alloy was 1009, 867, or 710 HV, respectively. During the compression tests at 25 °C, the AlCrFeTiCo alloy showed a peak strength of 3792 MPa, while the AlCrFeTiNi and AlCrFeTiCu alloys fractured at ~ 2300 MPa. At 600 °C, the AlCrFeTiCo alloy demonstrated the best performance, with the yield strength, peak strength, and plastic strain of 1960 MPa, 2121 MPa, and 1.8 %, respectively. The AlCrFeTiCu alloy also showed signatures of plasticity (~ 1 %) accompanied by a prominent strength reduction. The AlCrFeTiNi alloy remained brittle and fractured at 742 MPa.
- Microhardness dropped after annealing, and the annealing-induced decrease in microhardness was minor (< 10 %) in the AlCrFeTiCo and AlCrFeTiNi alloys, but it was noticeable (> 30 %) in the AlCrFeTiCu alloy. The annealing did not eliminate the room-temperature brittleness, but enhanced the mechanical properties at 600 °C. The AlCrFeTiCo alloy showed a 15 %-increase in yield strength (2264 MPa) and more than 2.5 times higher compressive plasticity (4.7 %). The AlCrFeTiNi alloy became more ductile (1 %) and stronger (2200 MPa). For the AlCrFeTiCu alloy, the annealing had a negative effect that resulted in a halved plasticity at 600 °C.
- The AlCrFeTiCo and AlCrFeTiNi alloys after annealing showed record-high specific yield strength values at 600 °C, which were 383 and 371 MPa*cm³/g, respectively. With these values, the AlCrFeTiCo and AlCrFeTiNi alloys outperformed all the LDMEAs/LDHEAs available in literature to date obtained both by SPS or conventional casting. The origin for such an outstanding strength was the synergistic effect of grain boundary strengthening and dominance of intermetallic phases in the structure.

CRedit authorship contribution statement

N. Stepanov: Writing – review & editing, Supervision. **D. Shaysultanov:** Investigation, Data curation. **E. Povolyaeva:** Visualization, Investigation, Data curation. **D. Moskovskikh:** Writing – review & editing, Resources, Data curation. **S. Zherebtsov:** Writing – review & editing. **Nikita Yu Yurchenko:** Writing – review & editing, Writing – original draft, Visualization, Validation, Data curation.

Declaration of Competing Interest

The authors declare that they have no known competing financial interests or personal relationships that could have appeared to influence the work reported in this paper.

Data availability

Data will be made available on request.

Acknowledgements

Funding: This work was supported by the Russian Science Foundation Grant no. 19–79–30066 (<https://rscf.ru/en/project/23-79-33001/>). A part of this research (SEM characterisation) was partially funded by the Ministry of Science and Higher Education of the Russian Federation as part of the World-Class Research Center program: Advanced Digital Technologies (Contract no. N^o 075–15–2022–312 dated 20.04.2022). The work was carried out using the equipment of the Joint Research Center of Belgorod State National Research University «Technology and Materials».

References

- X. Zhang, Y. Chen, J. Hu, Recent advances in the development of aerospace materials, *Prog. Aerosp. Sci.* 97 (2018) 22–34, <https://doi.org/10.1016/j.paerosci.2018.01.001>.
- E.A. Starke, J.T. Staley, Application of modern aluminum alloys to aircraft, *Prog. Aerosp. Sci.* 32 (1996) 131–172, [https://doi.org/10.1016/0376-0421\(95\)00004-6](https://doi.org/10.1016/0376-0421(95)00004-6).
- T. Dursun, C. Soutis, Recent developments in advanced aircraft aluminium alloys, *Mater. Des.* (1980–2015) 56 (2014) 862–871, <https://doi.org/10.1016/j.matdes.2013.12.002>.
- M. Peters, J. Kumpfert, C. h Ward, C. Leyens, Titanium alloys for aerospace applications, *Adv. Eng. Mater.* 5 (2003) 419–427, <https://doi.org/10.1002/adem.200310095>.
- D.B. Miracle, O.N. Senkov, A critical review of high entropy alloys and related concepts, *Acta Mater.* 122 (2017) 448–511, <https://doi.org/10.1016/j.actamat.2016.08.081>.
- M. Peters, D.B. Miracle, K.J. Chaput, J.P. Couzinie, Development and exploration of refractory high entropy alloys - A review, *J. Mater. Res.* 33 (2018) 3092–3128, <https://doi.org/10.1557/jmr.2018.153>.
- Z. Wang, S. Chen, S. Yang, Q. Luo, Y. Jin, W. Xie, L. Zhang, Q. Li, Light-weight refractory high-entropy alloys: A comprehensive review, *J. Mater. Sci. Technol.* 151 (2023) 41–65, <https://doi.org/10.1016/j.jmst.2022.11.054>.
- M.V. Kamal, S. Ragunath, M. Hema Sagar Reddy, N. Radhika, B. Saleh, Recent advancements in lightweight high entropy alloys – A comprehensive review, *Int. J. Lightweight Mater. Manuf.* 7 (2024) 699–720, <https://doi.org/10.1016/j.ijlmm.2024.06.001>.
- N.F. Lone, F. Czerwinski, D. Chen, Present challenges in development of lightweight high entropy alloys: A review, *Appl. Mater. Today* 39 (2024) 102296, <https://doi.org/10.1016/j.apmt.2024.102296>.
- O.N. Senkov, S.V. Senkova, D.B. Miracle, C. Woodward, Mechanical properties of low-density, refractory multi-principal element alloys of the Cr–Nb–Ti–V–Zr system, *Mater. Sci. Eng.: A* 565 (2013) 51–62, <https://doi.org/10.1016/j.msea.2012.12.018>.
- N.D. Stepanov, N.Y. Yurchenko, D.V. Skibin, M.A. Tikhonovsky, G.A. Salishchev, Structure and mechanical properties of the AlCr_xNbTiV (x = 0, 0.5, 1, 1.5) high entropy alloys, *J. Alloy. Compd.* 652 (2015) 266–280, <https://doi.org/10.1016/j.jallcom.2015.08.224>.
- N.Y. Yurchenko, N.D. Stepanov, D.G. Shaysultanov, M.A. Tikhonovsky, G. A. Salishchev, Effect of Al content on structure and mechanical properties of the Al_xCrNbTiVZr (x = 0; 0.25; 0.5; 1) high-entropy alloys, *Mater. Charact.* 121 (2016) 125–134, <https://doi.org/10.1016/j.matchar.2016.09.039>.
- N. Yurchenko, E. Panina, M. Tikhonovsky, G. Salishchev, S. Zherebtsov, N. Stepanov, Structure and mechanical properties of an in-situ refractory Al₂₀Cr₁₀Nb₁₅Ti₂₀V₂₅Zr₁₀ high entropy alloy composite, *Mater. Lett.* (2020) 127372, <https://doi.org/10.1016/j.matlet.2020.127372>.
- O.A. Waseem, H.J. Ryu, Combinatorial development of the low-density high-entropy alloy Al₁₀Cr₂₀Mo₂₀Nb₂₀Ti₂₀Zr₁₀ having gigapascal strength at 1000 °C, 155700–155700, *J. Alloy. Compd.* (2020), <https://doi.org/10.1016/j.jallcom.2020.155700>.
- R. Feng, C. Zhang, M.C. Gao, Z. Pei, F. Zhang, Y. Chen, D. Ma, K. An, J. D. Poplawsky, L. Ouyang, Y. Ren, J.A. Hawk, M. Widom, P.K. Liaw, High-throughput design of high-performance lightweight high-entropy alloys, *Nat. Commun.* 12 (2021) 4329, <https://doi.org/10.1038/s41467-021-24523-9>.
- M. Wang, Y. Lu, T. Wang, C. Zhang, Z. Cao, T. Li, P.K. Liaw, A novel bulk eutectic high-entropy alloy with outstanding as-cast specific yield strengths at elevated temperatures, *Scr. Mater.* 204 (2021) 114132, <https://doi.org/10.1016/j.scriptamat.2021.114132>.
- M. Wang, Y. Lu, J. Lan, T. Wang, C. Zhang, Z. Cao, T. Li, P.K. Liaw, Lightweight, ultrastrong and high thermal-stable eutectic high-entropy alloys for elevated-temperature applications, *Acta Mater.* 248 (2023) 118806, <https://doi.org/10.1016/j.actamat.2023.118806>.
- N. Yurchenko, E. Panina, D. Kapustin, V. Novikov, D. Volosevich, O. Klimova-Korsmik, G. Salishchev, S. Zherebtsov, N. Stepanov, A lightweight intermetallic Al–Cr–Ti medium-entropy alloy with good mechanical properties and oxidation resistance, *J. Alloy. Compd.* 967 (2023) 171865, <https://doi.org/10.1016/j.jallcom.2023.171865>.
- E. Nozdracheva, E. Panina, D. Volosevich, O. Klimova-Korsmik, G. Salishchev, S. Zherebtsov, N. Stepanov, N. Yurchenko, Effect of Fe and Mn on structure, mechanical properties, and oxidation resistance of lightweight intermetallic Al₅₅Cr₂₃Ti₂₂ complex concentrated alloy, *Intermetallics* 172 (2024) 108383, <https://doi.org/10.1016/j.intermet.2024.108383>.
- G. Diao, A. He, M. Wu, Y. Tang, W.G. Chen, Q.Y. Li, D. Li, Lightweight Al₃Ti-based medium-entropy alloys with well-balanced strength and ductility, *Scr. Mater.* 242 (2024) 115928, <https://doi.org/10.1016/j.scriptamat.2023.115928>.
- D.B. Miracle, Overview No. 104 The physical and mechanical properties of NiAl, *Acta Metall. Et. Mater.* 41 (1993) 649–684, [https://doi.org/10.1016/0956-7151\(93\)90001-9](https://doi.org/10.1016/0956-7151(93)90001-9).
- A. Lasalmonie, *Intermetallics: Why is it so difficult to introduce them in gas turbine engines?* *Intermetallics* 14 (2006) 1123–1129, <https://doi.org/10.1016/j.intermet.2006.01.064>.
- D.L. Davidson, K.S. Chan, D.L. Anton, The effects on fracture toughness of ductile-phase composition and morphology in Nb–Cr–Ti and Nb–Si in situ composites, *Met. Mater. Trans. A* 27 (1996) 3007–3018, <https://doi.org/10.1007/BF02663850>.
- J. Li, B. Liu, X. Zhang, L. Liu, G. Wilde, F. Ye, Bulk synthesis of Ti28Zr40Al20Nb12 high entropy alloy: a critical evaluation of processing conditions, *Appl. Phys. A* 129 (2023) 483, <https://doi.org/10.1007/s00339-023-06769-w>.

- [25] N.J. Welch, T.M. Butler, M.J. Quintana, P.C. Collins, The influence of microstructure on the oxidation behavior of a TaTiCr refractory complex concentrated alloy, *J. Alloy. Compd.* (2024) 175613, <https://doi.org/10.1016/j.jallcom.2024.175613>.
- [26] N.F. Shkodich, K.V. Kuskov, A.S. Sedegov, I.D. Kovalev, A.V. Panteleeva, Yu. S. Vergunova, Yu.B. Scheck, E. Panina, N. Stepanov, I. Serhienko, D. Moskovskikh, Refractory TaTiNb, TaTiNbZr, and TaTiNbZrX (X = Mo, W) high entropy alloys by combined use of high energy ball milling and spark plasma sintering: Structural characterization, mechanical properties, electrical resistivity, and thermal conductivity, *J. Alloy. Compd.* 893 (2022) 162030, <https://doi.org/10.1016/j.jallcom.2021.162030>.
- [27] Y. Zhang, Y. Ai, W. Chen, S. Ouyang, Preparation and microstructure and properties of AlCuFeMnTiV lightweight high entropy alloy, *J. Alloy. Compd.* 900 (2022) 163352, <https://doi.org/10.1016/j.jallcom.2021.163352>.
- [28] F. Gao, Y. Sun, L. Hu, J. Shen, W. Liu, M. Ba, C. Deng, Microstructure and strengthening mechanisms of novel lightweight TiAlV_{0.5}CrMo refractory high-entropy alloy fabricated by mechanical alloying and spark plasma sintering, *J. Alloy. Compd.* 932 (2023) 167659, <https://doi.org/10.1016/j.jallcom.2022.167659>.
- [29] C.O. Ujah, D.V.V. Kallon, V.S. Aigbodion, High entropy alloys prepared by spark plasma sintering: Mechanical and thermal properties, *Mater. Today Sustain.* 25 (2024) 100639, <https://doi.org/10.1016/j.mtsust.2023.100639>.
- [30] W. Lu, D. Liu, C. Wang, Q. An, R.O. Ritchie, L. Huang, S. Jin, N. Gao, L. Sun, L. Geng, New strategy in light-weight and ultrastrong Ti₄₀Nb₁₅Mo₃₀(NbCr)₁₅ refractory complex concentrated alloy, *Compos. Part B: Eng.* 281 (2024) 111555, <https://doi.org/10.1016/j.compositesb.2024.111555>.
- [31] D. Shaysultanov, A. Nepapushev, S. Zherebtsov, D. Moskovskikh, N. Stepanov, Structure and mechanical properties of a low-density AlCrFeTi medium entropy alloy produced by spark plasma sintering, *Mater. Sci. Eng.: A* 795 (2020) 140018, <https://doi.org/10.1016/j.msea.2020.140018>.
- [32] N.Y. Yurchenko, N.D. Stepanov, S.V. Zherebtsov, M.A. Tikhonovsky, G. A. Salishchev, Structure and mechanical properties of B2 ordered refractory AlNbTiVZr_x (x = 0–1.5) high-entropy alloys, *Mater. Sci. Eng. A* 704 (2017) 82–90, <https://doi.org/10.1016/j.msea.2017.08.019>.
- [33] K. Lee, Y. Jung, J. Han, S.H. Hong, K.B. Kim, P.K. Liaw, C. Lee, G. Song, Development of Precipitation-Strengthened Al_{0.8}NbTiVM (M = Co, Ni) Light-Weight Refractory High-Entropy Alloys, *Materials* 14 (2021) 2085, <https://doi.org/10.3390/ma14082085>.
- [34] H. Yao, Y. Liu, X. Sun, Y. Lu, T. Wang, T. Li, Microstructure and mechanical properties of Ti₃V₂NbAl_kNi_l low-density refractory multielement alloys, *Intermetallics* 133 (2021) 107187, <https://doi.org/10.1016/j.intermet.2021.107187>.
- [35] F. Xu, X. Gao, H. Cui, Q. Song, R. Chen, Lightweight and high hardness (AlNbTiVCr)_{100-x}Ni_x high entropy alloys reinforced by Laves phase, *Vacuum* 213 (2023) 112115, <https://doi.org/10.1016/j.vacuum.2023.112115>.
- [36] Q. Hu, H. Wang, L. Qian, L. Zeng, Q. Wang, X. Liu, Effects of Cu additions on microstructure and mechanical properties of as-cast CrFeCoNiCu_x high-entropy alloy, *Trans. Nonferrous Met. Soc. China* 33 (2023) 1803–1813, [https://doi.org/10.1016/S1003-6326\(23\)66223-5](https://doi.org/10.1016/S1003-6326(23)66223-5).
- [37] Y. Xie, Z. Xia, J. Hou, J. Xu, P. Chen, L. Wan, Effect of Co-Rich Phase Precipitation on the Microstructure and Mechanical Properties of CuCrNiCu_x Medium-Entropy Alloys Prepared via Laser Directed Energy Deposition, *Acta Metall. Sin. (Engl. Lett.)* 34 (2021) 1591–1600, <https://doi.org/10.1007/s40195-021-01316-z>.
- [38] P.H. Wu, N. Liu, W. Yang, Z.X. Zhu, Y.P. Lu, X.J. Wang, Microstructure and solidification behavior of multicomponent CoCrCu_xFeMoNi high-entropy alloys, *Mater. Sci. Eng.: A* 642 (2015) 142–149, <https://doi.org/10.1016/j.msea.2015.06.061>.
- [39] A. Raphael, S. Kumaran, K.V. Kumar, L. Varghese, Oxidation and corrosion resistance of AlCoCrFeTi high entropy alloy, *Mater. Today.: Proc.* 4 (2017) 195–202, <https://doi.org/10.1016/j.matpr.2017.01.013>.
- [40] Z.-S. Nong, Y.-N. Lei, J.-C. Zhu, Wear and oxidation resistances of AlCrFeNiTi-based high entropy alloys, *Intermetallics* 101 (2018) 144–151, <https://doi.org/10.1016/j.intermet.2018.07.017>.
- [41] J. Yi, L. Wang, M. Xu, L. Yang, Two new 3d transition metals AlCrCuFeTi and AlCrCuFeV high-entropy alloys: phase components, microstructures, and compressive properties, *Appl. Phys. A* 127 (2021) 74, <https://doi.org/10.1007/s00339-020-04212-y>.
- [42] C. Nagarjuna, S.K. Dewangan, H. Lee, K. Lee, B. Ahn, Exploring the mechanical and tribological properties of AlCrFeNiTi high-entropy alloy fabricated by mechanical alloying and spark plasma sintering, *Vacuum* 218 (2023) 112611, <https://doi.org/10.1016/j.vacuum.2023.112611>.
- [43] M. Wu, R.K. Sim, A. He, G. Diao, W. Chen, D. Chen, D. Li, Mechanisms underlying the influence of Co and Ti on the microstructure, mechanical and wear properties of A2/B2 typed AlCrFeNi alloy, *J. Alloy. Compd.* 968 (2023) 172070, <https://doi.org/10.1016/j.jallcom.2023.172070>.
- [44] A.S. Rogachev, D.O. Moskovskikh, A.A. Nepapushev, T.A. Sviridova, S. G. Vadchenko, S.A. Rogachev, A.S. Mukasyan, Experimental investigation of milling regimes in planetary ball mill and their influence on structure and reactivity of gasless powder exothermic mixtures, *Powder Technol.* 274 (2015) 44–52, <https://doi.org/10.1016/j.powtec.2015.01.009>.
- [45] C. Zhang, Y. Yang, The CALPHAD approach for HEAs: Challenges and opportunities, *MRS Bull.* 47 (2022) 158–167, <https://doi.org/10.1557/s43577-022-00284-8>.
- [46] K. Ishikawa, R. Kainuma and Kiyohito Ishida, M. Materials Science International Team, G. Effenberg, Al-Co-Ti Ternary Phase Diagram Evaluation · Phase diagrams, crystallographic and thermodynamic data: Datasheet from MSI Eureka in SpringerMaterials (https://materials.springer.com/msi/docs/sm_msi_r_10_010909_02), (n.d.). https://materials.springer.com/msi/docs/sm_msi_r_10_010909_02.
- [47] P.B. Budberg, M. Materials Science International Team, G. Effenberg, Al-Ni-Ti Ternary Phase Diagram Evaluation · Phase diagrams, crystallographic and thermodynamic data: Datasheet from MSI Eureka in SpringerMaterials (https://materials.springer.com/msi/docs/sm_msi_r_10_013824_01), (n.d.). https://materials.springer.com/msi/docs/sm_msi_r_10_013824_01.
- [48] R. Schmid-Fetzer, M. Materials Science International Team, G. Effenberg, Al-Cu-Ti Ternary Phase Diagram Evaluation · Phase diagrams, crystallographic and thermodynamic data: Datasheet from MSI Eureka in SpringerMaterials (https://materials.springer.com/msi/docs/sm_msi_r_10_016867_02), (n.d.). https://materials.springer.com/msi/docs/sm_msi_r_10_016867_02.
- [49] C.H. Liescher, V. Radmilovic, U. Dahmen, M. Asta, G. Ghosh, On the formation of hierarchically structured L21-Ni₂TiAl type precipitates in a ferritic alloy, *J. Mater. Sci.* 48 (2013) 2067–2075, <https://doi.org/10.1007/s10853-012-6980-3>.
- [50] G. Song, Z. Sun, B. Clausen, P.K. Liaw, Microstructural characteristics of a Ni₂TiAl-precipitate-strengthened ferritic alloy, *J. Alloy. Compd.* 693 (2017) 921–928, <https://doi.org/10.1016/j.jallcom.2016.09.177>.
- [51] S.-I. Baik, M.J.S. Rawlings, D.C. Dunand, Atom probe tomography study of Fe-Ni-Al-Cr-Ti ferritic steels with hierarchically-structured precipitates, *Acta Mater.* 144 (2018) 707–715, <https://doi.org/10.1016/j.actamat.2017.11.013>.
- [52] O.N. Senkov, S. Gorsse, D.B. Miracle, High temperature strength of refractory complex concentrated alloys, *Acta Mater.* 175 (2019) 394–405, <https://doi.org/10.1016/j.actamat.2019.06.032>.
- [53] J.D. Livingston, Laves-phase superalloys? *Phys. Status Solidi (a)* 131 (1992) 415–423, <https://doi.org/10.1002/pssa.2211310215>.
- [54] I. Moravcik, J. Cizek, J. Zapletal, Z. Kovacova, J. Vesely, P. Minarik, M. Kitzmantel, E. Neubauer, I. Dlouhy, Microstructure and mechanical properties of Ni_{1.5}Co_{1.5}CrFeTi_{0.5} high entropy alloy fabricated by mechanical alloying and spark plasma sintering, *Mater. Des.* 119 (2017) 141–150, <https://doi.org/10.1016/j.matdes.2017.01.036>.
- [55] B. Kang, J. Lee, H.J. Ryu, S.H. Hong, Microstructure, mechanical property and Hall-Petch relationship of a light-weight refractory Al_{0.1}CrNbVMo high entropy alloy fabricated by powder metallurgical process, *J. Alloy. Compd.* 767 (2018) 1012–1021, <https://doi.org/10.1016/j.jallcom.2018.07.145>.
- [56] Q. Liu, G. Wang, X. Sui, Y. Liu, X. Li, J. Yang, Microstructure and mechanical properties of ultra-fine grained MoNbTaTiV refractory high-entropy alloy fabricated by spark plasma sintering, *J. Mater. Sci. Technol.* 35 (2019) 2600–2607, <https://doi.org/10.1016/j.jmst.2019.07.013>.
- [57] M. Yamaguchi, Y. Umakoshi, The deformation behaviour of intermetallic superlattice compounds, *Prog. Mater. Sci.* 34 (1990) 1–148, [https://doi.org/10.1016/0079-6425\(90\)90002-Q](https://doi.org/10.1016/0079-6425(90)90002-Q).
- [58] E.M. Schulson, D.R. Barker, A brittle to ductile transition in NiAl of a critical grain size, *Scr. Metall.* 17 (1983) 519–522, [https://doi.org/10.1016/0036-9748\(83\)90344-7](https://doi.org/10.1016/0036-9748(83)90344-7).
- [59] Z.Y. Ding, Q.F. He, D. Chung, Y. Yang, Evading brittle fracture in submicron-sized high entropy intermetallics in dual-phase eutectic microstructure, *Scr. Mater.* 187 (2020) 280–284, <https://doi.org/10.1016/j.scriptamat.2020.06.032>.
- [60] N.S. Stoloff, R.G. Davies, The mechanical properties of ordered alloys, *Prog. Mater. Sci.* 13 (1968) 1–84, [https://doi.org/10.1016/0079-6425\(68\)90018-2](https://doi.org/10.1016/0079-6425(68)90018-2).
- [61] Y. Umakoshi, M. Yamaguchi, T. Yamane, Plastic deformation of Co₂AlTi, *Philos. Mag. A* 53 (1986) 221–232, <https://doi.org/10.1080/01418618608242822>.
- [62] S. Dasari, A. Jagetia, A. Sharma, M.S.K.K.Y. Nartu, V. Soni, B. Gwalani, S. Gorsse, R. Banerjee, Tuning the degree of chemical ordering in the solid solution of a complex concentrated alloy and its impact on mechanical properties, *Acta Mater.* 212 (2021) 116938, <https://doi.org/10.1016/j.actamat.2021.116938>.
- [63] N. Yurchenko, E. Panina, A. Tojibaev, S. Zherebtsov, N. Stepanov, Overcoming the strength-ductility trade-off in refractory medium-entropy alloys via controlled B2 ordering, *Mater. Res. Lett.* 10 (2022) 813–823, <https://doi.org/10.1080/21663831.2022.2109442>.
- [64] N. Yurchenko, E. Panina, A. Tojibaev, V. Novikov, G. Salishchev, S. Zherebtsov, N. Stepanov, Effect of B2 ordering on the tensile mechanical properties of refractory Al_xNb₄₀Ti₄₀V_{20-x} medium-entropy alloys, *J. Alloy. Compd.* 937 (2023) 168465, <https://doi.org/10.1016/j.jallcom.2022.168465>.
- [65] N. Yurchenko, E. Panina, S. Zherebtsov, N. Stepanov, Design and characterization of eutectic refractory high entropy alloys, 101057–101057, *Materialia* 16 (2021), <https://doi.org/10.1016/j.mtla.2021.101057>.
- [66] X.W. Liu, Z.C. Bai, X.F. Ding, J.Q. Yao, L. Wang, Y.Q. Su, Z.T. Fan, J.J. Guo, A novel light-weight refractory high-entropy alloy with high specific strength and intrinsic deformability, *Mater. Lett.* 287 (2021) 129255, <https://doi.org/10.1016/j.matlet.2020.129255>.
- [67] T. dang Huang, S. yu Wu, H. Jiang, Y. ping Lu, T. min Wang, T. ju Li, Effect of Ti content on microstructure and properties of Ti₂ZrVnB refractory high-entropy alloys, *Int. J. Miner., Metall. Mater.* 27 (10) (2020) 1318–1325, <https://doi.org/10.1007/S12613-020-2040-1>.
- [68] N.D. Stepanov, N.Y. Yurchenko, E.S. Panina, M.A. Tikhonovsky, S.V. Zherebtsov, Precipitation-strengthened refractory Al_{0.5}CrNbTi₂V_{0.5} high entropy alloy, *Mater. Lett.* 188 (2017) 162–164, <https://doi.org/10.1016/J.MATLET.2016.11.030>.
- [69] W. Jiang, X. Wang, H. Kang, B. Jiang, D. Dong, Y. Wang, D. Zhu, Microstructure and mechanical properties of AlNbTiVZr system refractory high entropy alloys, *J. Alloy. Compd.* 925 (2022) 166767, <https://doi.org/10.1016/j.jallcom.2022.166767>.